Order, disorder and mixing: The atomic structure of amorphous mixtures of titania and tantala

Riccardo Bassiri[a,*], Matthew R. Abernathy[b], Franklin Liou[a], Apurva Mehta[c], Eric K. Gustafson[b], Martin Hart[d], Hafizah N. Isa[d], Namjun Kim[e], Angie C. Lin[a], Ian MacLaren[d], Iain W. Martin[d], Roger K. Route[a], Sheila Rowan[d], Badri Shyam[c], Jonathan F. Stebbins[e], Martin M. Fejer[a]

[a] *E. L. Ginzton Laboratory, Stanford University, Stanford, CA 94305, USA*
[b] *LIGO Laboratory, California Institute of Technology, Pasadena, CA 91125, USA*
[c] *Stanford Synchrotron Radiation Lightsource, SLAC National Accelerator Laboratory, Menlo Park, CA 94025, USA*
[d] *SUPA, School of Physics and Astronomy, University of Glasgow, Glasgow, G12 8QQ, United Kingdom*
[e] *Department of Geological Sciences, Stanford University, Stanford, CA 94305, USA*

Abstract

The atomic structure of mixtures of titania (TiO_2) and tantala (Ta_2O_5) ion-beam sputtered amorphous thin film coatings at various post-deposition annealing temperatures have been studied using Ta L_{III} and Ti K edge Extended X-ray Absorption Fine Structure (EXAFS). The results indicate that post-deposition annealing produces subtle changes in the short range order (< 1 nm) for samples which remain amorphous. We also show that titania-tantala mixtures maintain a structure similar to that of pure tantala, with the titanium atoms preferring to sit at the second shell distance, which is similar to the Ta-Ta distance seen in the pure tantala structure. A discussion is also included on interpretation of the general trends identified in the EXAFS data and how this relates to previous and ongoing studies of the structure and mechanical loss measurements of titania-tantala coatings.

1. Introduction

Thin film coatings of amorphous heavy metal oxides such as amorphous tantalum pentoxide (a-Ta_2O_5), otherwise known as tantala, are commonly used as high-refractive-index materials in many high-precision optical applications. Tantala is known for its low optical absorption and relatively high index contrast with silica [1] making the material extremely useful in optical atomic clocks [2], ring laser gyroscopes [3], frequency combs [4, 5], and high-precision interferometers such as the Laser Interferometer Gravitational-wave Observatory (LIGO) [6]. However, in many of these cases, the tantala layers are a limiting source of Brownian thermal noise, which is directly related to the mechanical loss (internal friction) of the material. [7].

Previous research has shown that variations in mixing with other materials and post-deposition annealing can noticeably change both the optical and mechanical properties of ion beam sputtered (IBS) tantala thin films [8–10]. It is speculated that these changes come about due to increased oxygen bonding and increased constraints on the so-called two-level-systems responsible for mechanical loss [11, 12].

In order to fully understand why these manufacturing conditions alter the thin film properties, and to inform studies that aim to further improve their performance, it has become necessary to understand the nature of the changes at the level of their atomic structures.

Changes in the atomic structure of amorphous tantala due to annealing may include reduction of oxygen deficiencies and increased local order [13]. Recently, studies using Transmission Electron Microscopy have probed the short range order of tantala [14] and shown a correlation between short range order and mechanical loss [15] in titania and tantala mixtures. These atomic structure investigations have demonstrated that a detailed understanding of the structural changes on the nano-scale may reveal the origins of the mechanical loss, and help inform various atomic modeling efforts. Additionally, a previous report using Ta L_{III} EXAFS measurements gives detailed information on the local structure of pure tantala annealed at various temperatures [16].

The work presented here builds upon this previous research by using Ta L_{III} and Ti K EXAFS to analyze the short range order of mixtures of titania and tantala ion-beam sputtered thin films, with titania concentrations of 14%, 52%, and 68% by cation percentage. Data from pure tantala and pure titania samples are also given for comparison.

2. Experimental setup

The samples in our study are single-layer 500 nm-thick IBS thin film coatings of amorphous tantala mixed with titania (a-Ti:Ta_2O_5) deposited by the Australian Centre for Precision Optics (ACPO, Lindfield, Australia) on 1 inch

*Corresponding author:
Email address: rbassiri@stanford.edu (Riccardo Bassiri)

diameter fused silica substrates. After deposition, the samples were annealed for 24 hours in air at 300°C and 600°C, some were also left unannealed in their as-deposited (AD) state. A pure unannealed IBS titania sample was also measured and was deposited by MLD Technologies (Mountain View, California).

Samples were measured using Electron Energy Loss Spectroscopy (EELS) to have titania cation concentrations of 0, 14±3, 52±10 and 68±1%. Some of the samples were back-thinned to reduce the substrate thickness from 6.35 mm to ∼0.1 mm, allowing for some EXAFS data to be taken in transmission. In this article, we will refer to samples using their titania cation concentration and annealing temperature, therefore, the 52% titania sample that was annealed to 300°C will be referred to as the 52% Ti 300°C sample.

The samples were characterized at beamline 4-3 at the Stanford Synchrotron Radiation Lightsource (SSRL), which is a dedicated X-ray Absorption Spectroscopy (XAS) beamline. A standard experimental setup was used, which allowed for simultaneous collection of the data in both fluorescence and transmission modes. The Ta L_{III} absorption edge has an energy of 9881 eV, and spectra were collected over an energy range of 9700 eV to 11020 eV. Additionally, EXAFS spectra were taken on the Ti K absorption edge, which has an energy of 4966 eV, and data were collected over an energy range of 4735 eV to 5900 eV. The data from the samples were studied in both fluorescence and transmission, and it was determined that self-absorption in fluorescence mode was negligible. Ultimately, fluorescence data for the samples were analyzed, as it had a higher signal-to-noise ratio (SNR).

3. Data analysis procedure

Analysis of the EXAFS absorption data was done similarly to that described in recent work by Bassiri *et al.*[16]. As is standard for EXAFS data, the information on the nearest neighbor distribution is given by the oscillatory part of the absorption coefficient above an absorption edge. The raw EXAFS data is converted from energy space to k-space, and is normally represented as the function $\chi(k)$, which can be Fourier transformed to give a distribution in real space, R-space, denoted as $\chi(R)$.

The EXAFS background subtraction and data extraction was done using the Athena data analysis package [17]. Fourier transformation to R-space was done using a k^3 weighing and Hanning windowing over the k-range of 3 to 14 Å^{-1} for the Ta L_{III} edge and 3 to 10 Å^{-1} for Ti K edge.

IFEFFIT [18] was used for fitting to the $\chi(R)$ data, with three free parameters per path and an additional parameter for the absorption energy. The data were fit using a ΔR between 1 and 4 Å for both the Ta L_{III} and Ti K edges. For the Δk ranges, 3 to 14 Å^{-1} and 3 to 10 Å^{-1} were used for Ta L_{III} and Ti K edges respectively. Only single scattering paths were used in the fits, as no significant multiple-scattering paths were identified.

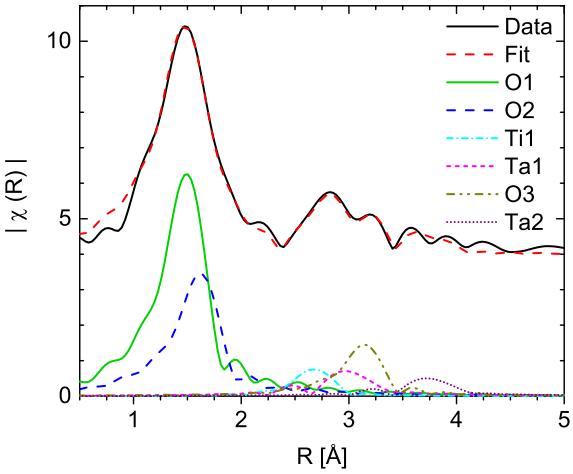

Figure 1: Partial EXAFS $\chi(R)$ plot from the FEFF fit of the Ta L_{III} edge of the 14% Ti AD sample.

Theoretical standards were generated by performing *ab initio* calculations of EXAFS spectra from single-atom scattering using the standard EXAFS formula [19], with the fit parameters given in Table 1. The MSRD, σ_i^2, measures the mean-square-relative-displacement in the bond distance. In some fits, σ_i^2 was subject to additional constraints, such as requiring that the MSRD of scatterers be equal to those of closer ones (shown as the dash '–' in Table 2). The absorption energy, E_0, is a fit to the true energy of the absorption edge, to make up for variation in calibration and energy shift due to bonding conditions. E_0 is only fit once per spectra. The number of scatterers at a distance R_i is probed by the parameter $N_i S_0^2$. Ideally, the value on N_i would give the number of atoms at this distance, but difficulties arise in separation from the value of S_0^2. While the value of S_0^2 is generally between 0.8 and 1.0, additional systematic errors that arise when fitting to amorphous samples, and large correlations between the value of N_i and other parameters lead to real uncertainties sometimes greater than 15% [20, 21]. In the tables found in Sections 4, we give both NS_0^2 and $N(S_0^2 = 0.8)$ with the associated errors from the IFEFFIT fit, however, these numbers should not be regarded as an exact measurement, given the limitations described here.

Table 1: Description of fit parameters in fitting EXAFS data to *ab-initio* models.

Fit Parameter	Description
$N_i S_0^2$	Total scattering Amplitude
R_i	Distance to scatterer
σ_i^2	Mean Square Relative Displacement (MSRD)
E_0	Absorption Energy

4. Results and Analysis

4.1. Model fitting to Ta L_{III} Edge

Fig. 1 shows the resulting best fit to data taken on the Ta L_{III} edge of the 14% Ti AD sample. The Fourier Transform of $\chi(k)$ spectra, $\chi(R)$, is a representation of nearest

neighbor distributions. The peaks are usually shifted by 0.3-0.4 Å to lower R values due to a phase shift of the electron wavefunction in the scattering process. From this figure, one can see which features within the $\chi(R)$ plots are associated with which atoms in the fit model. The atomic shell model was chosen based on that from Bassiri *et al.*[16] as this model might be expected to fit at least the data from the 14% Ti samples, and any deviations could be attributed to the addition of titanium. In the Bassiri model, the first shell is a split shell of oxygen atoms (O1 and O2) located roughly 1.9 Å from the central tantalum atom, the second shell is composed of a tantalum atom (Ta1), and the third shell is another oxygen atom (O3). Finally, a fourth-shell tantalum atom (Ta2) is visible at roughly the position one would expect from a 180-degree Ta-O-Ta bond, at ∼3.9 Å.

Due to constraints on the allowable number of fit parameters, only one titanium atom could be fitted, and the ∼3 Å location was the only position where a titanium atom would fit to the data. This may be taken as a strong indication that this is the true location of titanium within the Bassiri model. This also seems to indicate that the titanium atoms prefer a radial distance similar to those of the Ta1 atoms.

Looking at the values of NS_0^2, given in Table 2, we can draw some conclusions on the effects of the addition of titanium atoms into the tantala. In agreement with the Bassiri model, the sum of the $N(S_0^2 = 0.8)$ values of first-shell oxygen atoms surrounding the central tantalum atoms was 4-5, and this did not change significantly with the addition of titanium atoms into the material. The partial crystallization of the 68% Ti 600°C sample did, however lead to an increase in first-shell oxygen atoms, with the sum being 5.31(54), much larger than in any other sample.

The value of NS_0^2 of the second-shell tantalum atoms has a large uncertainty associated with it, due to the influence of the nearby oxygen and titanium scatterers in the $\chi(R)$ plots, but the number appears to be unaffected by the concentration of titanium atoms, aside from the possible difference between pure tantala annealed at 300°C and any other sample. This would appear to indicate that while the titanium atoms prefer the Ta1 position, they do not replace the Ta1 atoms. This can be seen more clearly in Fig. 2, where the number of Ta atoms (from the last column of Table 2) at the 3.1 Å position is plotted against the number of Ti atoms at the same position for various annealing temperatures. The values for the 68% Ti samples are not included due to the large uncertainty in their fit values. However, it is not clear what the mechanism for this is: such an increase in metal atoms within the vicinity of the central tantalum atom would be expected to change the oxygen coordination and atomic distances, which is an effect that we do not see. In this particular case it is not possible to fully differentiate between the number of second shell metal atoms, however it is clear that Ti is placed in the second nearest neighbor (Ta-O-Ti) position.

Table 2: Ta L_{III} edge EXAFS fits for the titania doped tantala samples. Uncertainties given in the parentheses represent uncertainty from the smallest significant figure.

Scattering Path	R	σ^2	NS_0^2	$N(S_0 = 0.8)$
		14% Ti AD		
Ta-O1	1.88(2)	0.0056(16)	2.22(45)	2.78(56)
Ta-O2	2.00(2)	–	1.41(24)	1.76(30)
Ta-Ta1	3.12(3)	0.0031(42)	0.18(31)	0.23(38)
Ta-O3	3.52(2)	–	1.98(52)	2.47(65)
Ta-Ta2	3.87(2)	–	0.23(26)	0.29(33)
Ta-Ti1	3.06(3)	0.0034(95)	0.21(33)	0.26(42)
		52% Ti AD		
Ta-O1	1.88(2)	0.0066(17)	2.17(41)	2.71(52)
Ta-O2	2.00(2)	–	1.88(30)	2.35(37)
Ta-Ta1	3.14(3)	0.0089(38)	0.65(55)	0.81(69)
Ta-O3	3.53(2)	–	1.95(48)	2.43(60)
Ta-Ta2	3.88(3)	–	0.58(50)	0.72(63)
Ta-Ti1	3.10(3)	–	0.55(26)	0.68(33)
		68% Ti AD		
Ta-O1	1.89(2)	0.0050(19)	2.05(36)	2.57(45)
Ta-O2	2.03(2)	–	2.06(31)	2.58(38)
Ta-Ta1	3.21(3)	0.0164(63)	5.33(350)	6.66(437)
Ta-Ta2	3.86(5)	–	2.16(293)	2.70(366)
Ta-O3	3.62(6)	–	1.07(125)	1.34(156)
		0% Ti 300°C		
Ta-O1	1.86(0)	0.0036(5)	2.23(13)	2.78(17)
Ta-O2	2.01(1)	–	1.75(8)	2.19(10)
Ta-Ta1	3.13(1)	0.0066(15)	0.90(30)	1.13(37)
Ta-Ta2	3.88(2)	–	0.43(21)	0.54(27)
Ta-O3	3.55(1)	–	2.24(24)	2.81(30)
		14% Ti 300°C		
Ta-O1	1.88(1)	0.0050(14)	2.24(39)	2.80(49)
Ta-O2	2.01(2)	–	1.37(19)	1.71(23)
Ta-Ta1	3.11(4)	0.0027(48)	0.14(24)	0.17(30)
Ta-Ta2	3.88(2)	–	0.24(30)	0.30(38)
Ta-O3	3.54(2)	–	1.99(53)	2.49(67)
Ta-Ti1	3.07(3)	0.0049(97)	0.27(40)	0.34(50)
		52% Ti 300°C		
Ta-O1	1.85(2)	0.0153(19)	-8.65(1199)	-10.82(1499)
Ta-O2	1.89(3)	–	12.30(1184)	15.37(1480)
Ta-Ta1	3.12(18)	0.0101(73)	0.24(61)	0.31(76)
Ta-Ta2	3.88(4)	–	0.70(103)	0.88(129)
Ta-O3	3.52(7)	–	3.55(96)	4.44(120)
Ta-Ti1	3.11(4)	–	0.85(82)	1.06(102)
		68% Ti 300°C		
Ta-O1	1.89(1)	0.0054(11)	2.14(24)	2.67(30)
Ta-O2	2.02(1)	–	1.95(17)	2.43(21)
Ta-Ta1	3.16(1)	0.0209(42)	15.16(1158)	18.95(1447)
Ta-Ta2	3.84(2)	–	5.43(449)	6.79(561)
Ta-O3	3.56(2)	–	2.07(68)	2.59(85)
Ta-Ti1	3.02(2)	–	-4.75(413)	-5.94(516)
		0% Ti 600°C		
Ta-O1	1.87(1)	0.0037(16)	2.19(39)	2.74(48)
Ta-O2	2.01(2)	–	1.67(21)	2.08(26)
Ta-Ta1	3.13(23)	0.0003(672)	0.07(157)	0.09(196)
Ta-Ta2	3.81(5)	0.0361(115)	37.72(4306)	47.15(5383)
Ta-O3	3.53(10)	–	-2.64(681)	-3.30(851)
Ta-Ta3	3.44(4)	0.0088(120)	-3.29(954)	-4.11(1192)
		14% Ti 600°C		
Ta-O1	1.88(2)	0.0055(16)	2.33(47)	2.92(59)
Ta-O2	2.01(2)	–	1.37(24)	1.71(30)
Ta-Ta1	3.10(5)	0.0007(56)	0.07(13)	0.09(16)
Ta-O3	3.54(2)	–	2.15(54)	2.68(67)
Ta-Ta2	3.87(2)	–	0.17(26)	0.22(33)
Ta-Ti1	3.08(3)	0.0057(89)	0.32(39)	0.40(49)
		52% Ti 600°C		
Ta-O1	1.90(1)	0.0058(16)	2.29(36)	2.86(45)
Ta-O2	2.03(2)	–	1.96(24)	2.45(30)
Ta-Ta1	3.19(3)	0.0081(43)	0.69(48)	0.86(59)
Ta-O3	3.57(3)	–	1.50(58)	1.87(72)
Ta-Ta2	3.86(3)	–	0.54(53)	0.67(67)
Ta-Ti1	3.12(2)	–	0.81(40)	1.02(51)
		68% Ti 600°C		
Ta-O1	1.94(1)	0.0080(11)	5.06(51)	6.33(63)
Ta-Ti1	3.13(2)	0.0071(30)	2.22(109)	2.77(136)
Ta-Ta1	3.12(4)	0.0167(62)	6.20(370)	7.75(463)
Ta-Ti2	3.87(1)	0.0016(25)	0.98(49)	1.22(61)

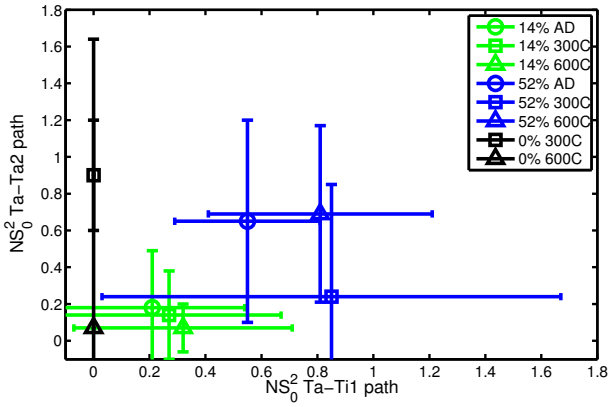

Figure 2: Plot of the NS_0^2 value for Ta atoms from the Ta L_{III} EXAFS fits at the 3.1 Å position is plotted against the NS_0^2 value of Ti atoms at the same position for various annealing temperatures.

From the parameter values given in Table 2, it is evident that the large number of fit parameters and correlations between parameters (not shown) allows for large uncertainties, making it difficult to extract quantitative changes due to titania concentration and annealing temperature. However, one can see qualitative differences in both the $\chi(k)$ and $\chi(R)$ data that appear to be significant.

4.2. Qualitative Analysis of Ta L_{III} Edge

Given the radial association between the $\chi(R)$ and atomic model seen in Fig. 1, we can qualitatively interpret the changes seen as being effected by changes in the distribution of the associated model atoms. Fig. 3 shows the Ta L_{III} $\chi(R)$ and $\chi(k)$ spectra as a function of titania concentration separated by annealing temperature, and clearly identifies significant changes to the short range order around the Ta species as a function of titania concentration.

The most noticeable changes in the structure with increasing titania concentration occur in the second shell. As expected, Fig. 3 (b) shows the peak at 2.8 Å, where Ti1 distance is located, growing as titania concentration is increased. The associated decrease in the shoulder and higher R oscillations may be partly due to the dominance of the Ti1 atom, but may also represent a drop in the second shell oxygen co-ordination with high titania concentration. In general, it appears as though, with the exception of the 68% Ti 600°C sample, Ti mixing decreases the order in the longer range distances, or at least reduces their co-ordination within the second shell.

From both the $\chi(R)$ and $\chi(k)$ plots it is also apparent that the 68% Ti 600°C sample has at least partially crystallized. This is evidenced by the significant increase in signal at high k-space and larger co-ordination in R-space. This has also been confirmed with selected area electron diffraction images, which show sharp crystalline Bragg spots.

There are also some subtle changes in the first shell Ta-O distance (O1 and O2), which appears to increase–possibly indicating a higher O2 population–with increasing titania concentration for the annealed samples. This can be more clearly identified in Fig. 4, by tracing the movement of the first peak to higher R values as the titania concentration increases. Fig. 4 shows the $\chi(R)$ and $\chi(k)$ Ta L_{III} spectra as a function of annealing temperature, separated by titania concentration. The higher O2 population is also supported by the growth of the shoulder on the first shell peaks in Fig. 3 with increasing titania concentration. It is interesting to note that this is not supported by the fits to the Bassiri model, however, the O1 and O2 NS_0^2 values are highly correlated in the fits, making it difficult to separate the number of atoms in each population.

As a function of annealing temperature, each titania concentration shows mostly subtle changes in the local atomic structure. The general trend of increasing peak heights in the $\chi(r)$ plots (Fig. 4(b)), indicates an increase in local order, as one might expect as the samples approach an annealing temperature that will induce crystallization. Again, this is evident in the 68% Ti 600°C sample which has at least partially crystallized, and highlights the increased local order affect as a function of annealing temperature. Generally, it appears that changes in the local order with annealing become more apparent as titania concentration is increased. Very little change is visible in the pure samples, while there are noticeable increases in O3 distribution and Ti1 peak in the 52% Ti samples with increasing annealing temperature.

For the 14% Ti samples, the second shell O3 shows a clear increase in order with increasing annealing temperature. It should be noted that while these changes are clear in R-space, they are less so in k-space. However, the $\chi(k)$ data for the 14% Ti samples have the best SNR, so this may be a real change and is possibly not seen in the other mixtures due to lower SNR.

4.3. Model fitting to Ti K Edge

The model fits to the Ti K edge, an example of which is seen in Fig. 5, were less revealing than those to the Ta L_{III} edge, given the relative weakness of the Ti K edge absorption strength. In addition, significantly fewer spectra were taken, leaving a lower SNR for these lines. This resulted in noisier average spectra, as seen in Figs. 6 and 7, and Fourier transforms out to a k of only 10 Å^{-1}. The associated $\chi(R)$ plots show significantly fewer features.

In fitting to the Ti K edge data, we attempted to fit three models: 1) Ti-O and Ti-Ti, 2) Ti-O and Ti-Ta, and 3) Ti-O, Ti-Ta, and Ti-Ti. Model 3 proved impossible to fit with one metal atom always dominating over the other and forcing the parameters of the other into nonphysical values. However, both models 1 and 2 fit reasonably well, as can be seen in Fig. 5. In the case of the partially crystallized 68% Ti 600°C sample, we were also able to fit a third-shell oxygen atom. The results of these model fits can be seen in Tables 3, and 4. To compare the effectiveness of the various models, we can construct a ratio of the χ^2 values

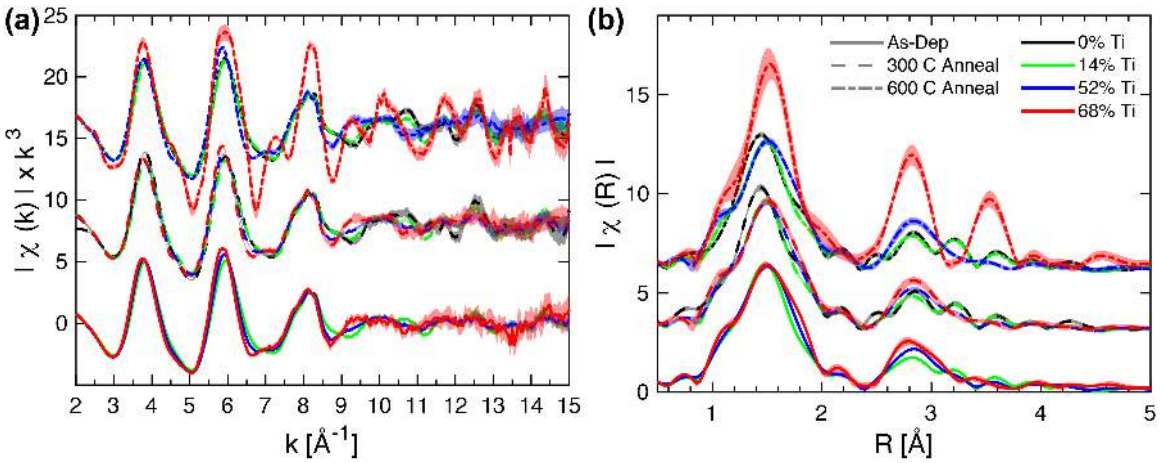

Figure 3: Ta L_{III} EXAFS (a) $\chi(k)$ and (b) $\chi(R)$ plots, where the different annealing temperatures are offset.

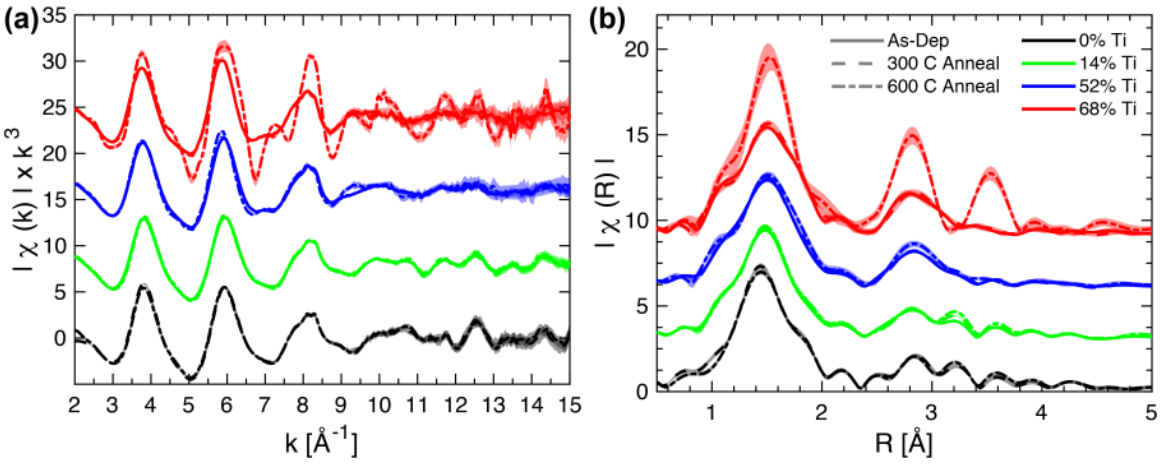

Figure 4: Ta L_{III} EXAFS (a) $\chi(k)$ and (b) $\chi(R)$ plots, where the different titania concentrations are offset.

minimized during the fit procedure: $r\chi^2 = \chi_2^2/\chi_1^2$, where the subscripts match the associated models.

In general, Model 1 produces a better fit to the data than model 2, with an average $r\chi^2$ of 1.29; however, in all of the 14% Ti samples, model 2 is favored over model 1. In the case of these lower-Ti samples, the average value of $r\chi^2$ is 0.86. This is not surprising, as one would expect these samples to be mostly tantala, with each Ti atom unlikely to see another Ti atom. In the remaining samples, there does not appear to be any trend in $r\chi^2$ with increasing titania concentration with an average value of $r\chi^2$ of 1.47.

It is clear that the Ti K edge data cannot resolve the difference between the Ti-Ti and Ti-Ta paths. This is particularly evident when considering that the fit of model 1 to the pure titania sample is only slightly favored over the fit of model 2 ($r\chi^2 = 1.11$). This is consistent with the Ta L_{III} data, which indicates that there are metal second nearest neighbours to Ti atoms, many of which will be Ta atoms and some may be Ti atoms at higher Ti concentrations. We therefore refer to the second shell atom only as the metal atom, occurring at a distance of around 3.1 - 3.2 Å, as we are unable to discriminate between the two.

The first shell oxygen path is unaffected by the fit to the second-shell metal path, allowing some analysis of the trends in the oxygen atom as probed by the Ti absorption. From this, one can see that the first shell oxygen is not strongly affected by annealing or titania concentration, and has a radial distance value of approximately 1.9 Å. Interestingly, the fits indicated that the O1 NS_0^2 values decrease with increasing titania concentration, and the trend is statistically significant at the 95% confidence level. However, this is not in agreement with recent findings in NMR data, which show increasing oxygen coordination with increasing titania concentration for titania and tantala mixtures of sol-gel material [22].

4.4. Qualitative Analysis of Ti K Edge

For the 14% Ti samples the Ti K EXAFS data is particularly noisy, due to the low concentration of titania resulting in lower SNR in the data collection. Despite this, it is possible to identify systematic changes in the structure as a function of titania concentration, as can be seen in the EXAFS $\chi(k)$ and $\chi(R)$ plots in Fig. 6. The 52%,

Table 3: Model 1 (M1) Ti K edge EXAFS fits for the titania doped tantala samples. Uncertainties given in the parentheses represent uncertainty from the smallest significant figure.

Scattering Path	R	σ^2	NS_0^2	$N(S_0 = 0.8)$
		14% Ti AD		
Ti-O	1.89(1)	0.0137(20)	3.31(47)	4.13(59)
Ti-Ti	3.11(3)	-0.0003(83)	0.15(16)	0.18(20)
		52% Ti AD		
Ti-O	1.91(1)	0.0120(20)	2.89(41)	3.61(51)
Ti-Ti	3.09(3)	0.0070(78)	0.39(31)	0.49(39)
		68% Ti AD		
Ti-O	1.92(1)	0.0106(18)	2.72(37)	3.40(47)
Ti-Ti	3.08(2)	0.0078(68)	0.50(34)	0.62(42)
		100% Ti AD		
Ti-O	1.93(0)	0.0097(16)	2.63(31)	3.29(38)
Ti-Ti	3.08(0)	0.0068(50)	0.57(29)	0.71(37)
		14% Ti 300°C		
Ti-O	1.88(1)	0.0128(22)	3.30(53)	4.12(66)
Ti-Ti	3.10(4)	0.0119(128)	0.48(54)	0.60(68)
		52% Ti 300°C		
Ti-O	1.91(1)	0.0115(20)	2.88(43)	3.60(54)
Ti-Ti	3.09(3)	0.0100(88)	0.53(43)	0.66(54)
		68% Ti 300°C		
Ti-O	1.92(1)	0.0109(20)	2.65(40)	3.32(49)
Ti-Ti	3.09(3)	0.0080(68)	0.50(34)	0.62(42)
		14% Ti 600°C		
Ti-O	1.88(2)	0.0145(24)	3.65(62)	4.56(77)
Ti-Ti	3.09(4)	0.0106(107)	0.49(49)	0.62(61)
		52% Ti 600°C		
Ti-O	1.91(1)	0.0112(18)	2.88(38)	3.60(47)
Ti-Ti	3.10(2)	0.0084(69)	0.51(34)	0.63(43)
		68% Ti 600°C		
Ti-O	1.96(3)	0.0058(36)	3.26(103)	4.07(128)
Ti-Ti	3.08(17)	0.0126(291)	5.15(2216)	6.44(2770)
Ti-O	3.29(15)	0.0195(859)	13.06(1603)	16.32(2003)

Table 4: Model 2 (M2) Ti K edge EXAFS fits for the titania doped tantala samples. Uncertainties given in the parentheses represent uncertainty from the smallest significant figure.

Scattering Path	R	σ^2	NS_0^2	$N(S_0 = 0.8)$
		14% Ti AD		
Ti-O	1.88(1)	0.0142(20)	3.45(48)	4.32(60)
Ti-Ta	3.18(3)	0.0103(86)	0.84(84)	1.05(104)
		52% Ti AD		
Ti-O	1.91(2)	0.0120(24)	2.90(50)	3.63(62)
Ti-Ta	3.20(4)	0.0175(126)	1.71(201)	2.14(251)
		68% Ti AD		
Ti-O	1.92(2)	0.0105(24)	2.70(48)	3.38(60)
Ti-Ta	3.19(4)	0.0180(118)	2.10(228)	2.63(285)
		100% Ti AD		
Ti-O	1.92(2)	0.0094(27)	2.61(54)	3.27(68)
Ti-Ta	3.16(4)	0.0129(103)	1.68(182)	2.10(228)
		14% Ti 300°C		
Ti-O	1.88(1)	0.0130(20)	3.35(49)	4.19(61)
Ti-Ta	3.20(3)	0.0166(105)	1.62(165)	2.03(206)
		52% Ti 300°C		
Ti-O	1.91(2)	0.0116(23)	2.90(49)	3.62(62)
Ti-Ta	3.20(4)	0.0195(122)	2.22(241)	2.78(301)
		68% Ti 300°C		
Ti-O	1.92(2)	0.0110(25)	2.67(52)	3.34(65)
Ti-Ta	3.21(4)	0.0203(128)	2.51(280)	3.13(350)
		14% Ti 600°C		
Ti-O	1.87(1)	0.0147(22)	3.72(57)	4.64(71)
Ti-Ta	3.19(3)	0.0151(89)	1.61(145)	2.01(181)
		52% Ti 600°C		
Ti-O	1.91(1)	0.0114(22)	2.92(47)	3.65(59)
Ti-Ta	3.21(4)	0.0189(108)	2.29(222)	2.86(277)
		68% Ti 600°C		
Ti-O	1.94(3)	0.0062(39)	3.72(139)	4.64(174)
Ti-Ta	3.13(5)	0.0179(122)	13.57(2584)	16.96(3230)
Ti-O	3.19(9)	0.0356(774)	21.06(4962)	26.32(6202)

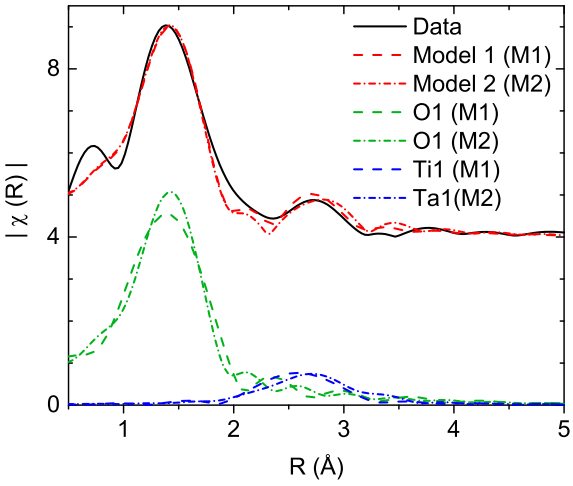

Figure 5: Partial EXAFS $\chi(R)$ plot from the FEFF fit of the Ti K edge of the 52% Ti 300°C sample. The figure shows two fits, model 1 (M1) and model 2 (M2), where the metal atom in the second shell is either Ti (M1) or Ta (M2).

68% and 100% Ti samples have good quality data for the region of $k < 10$ Å^{-1}.

The Ti-O distance shows subtle changes with increasing titania content, indicating a slightly longer Ti-O distance with increasing titania content, which is also borne out in the model fits. As with the Ta L_{III} data, the majority of changes in the local structure occur beyond the first shell, where increasing titania content increases the co-ordination of the Ti-metal scattering paths. Interestingly, the data from a pure titania sample yields a nearest neighbor distribution that is very similar to the mixed titania-tantala samples, fitting in well with the changes in structure seen with increasing Ti content.

Fig. 7 shows the changes in Ti K EXAFS as a function of annealing temperature, and, as with Ta L_{III} data, indicates some subtle changes in the short range structure for the samples which have stayed amorphous. In particular, the changes appear to be most apparent in the 52% and 68% Ti samples (there was only one 100% Ti AD sample), and concentrated in the first shell Ti-O scattering path. However, the change is not consistent with increasing annealing temperature for the 52% Ti sample. and it was also not possible to get any direct indication of the changes in co-ordination from the fits.

As with the Ta L_{III} data, we see further confirmation that the 65% Ti 600°C sample has partially crystallized, with both $\chi(k)$ and $\chi(R)$ showing greatly increased local order.

5. Discussion

As we have already mentioned in previous sections, the fitted parameters from the EXAFS data are not sensitive enough to extract all of the qualitative differences observed in the $\chi(R)$. However, we can discuss the general trends that exist within the fits and the consequences for our

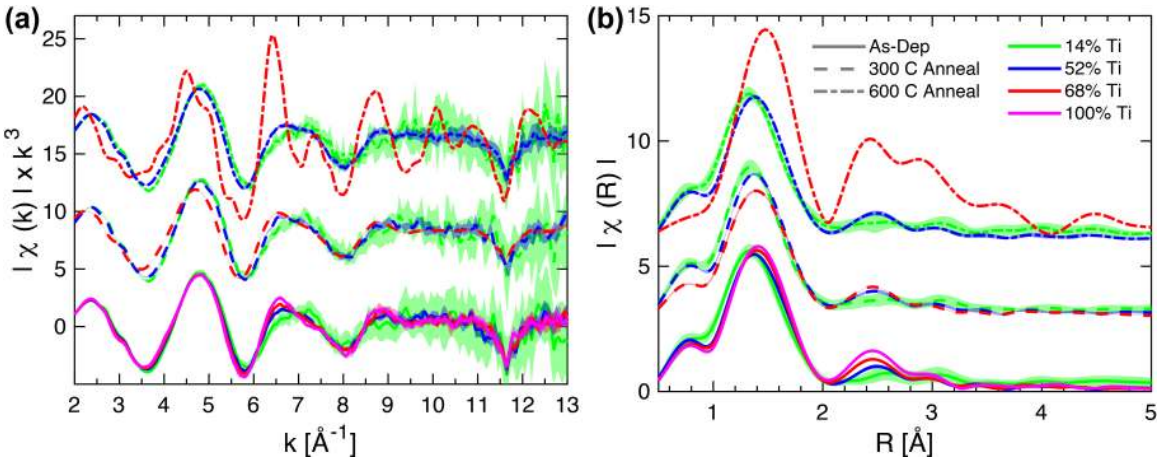

Figure 6: Ti K EXAFS (a) $\chi(k)$ and (b) $\chi(R)$ plots, where the different annealing temperatures are offset.

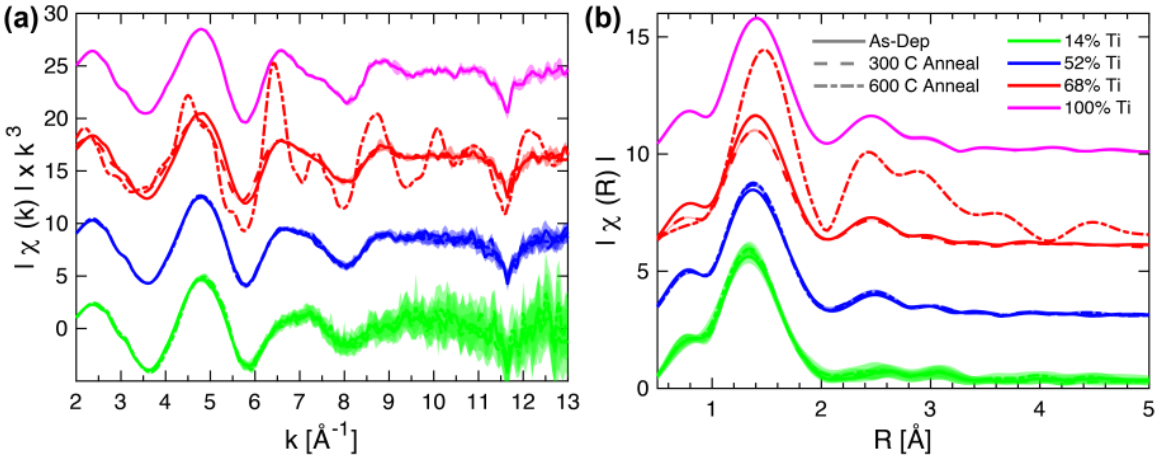

Figure 7: Ti K EXAFS (a) $\chi(k)$ and (b) $\chi(R)$ plots, where the different titania concentrations are offset.

understanding of the local atomic structure, and how this relates to mechanical loss.

The EXAFS $\chi(R)$ data does hint at increased local order with increasing annealing temperature, especially in the 3.5 Å O3 distance. This subtle change with annealing is predicted by previous studies of the short range order of tantala based coatings [14, 16]. For 14% Ti samples, the peak at 3.1 Å increases in amplitude with temperature. Extrapolation from the fits indicates that the feature is due to changing Ti/Ta ratio in the second shell. In 52% Ti samples, changes are also seen in the second shell. The sample annealed at 600°C exhibits different behavior in the second shell tantalum and third shell (oxygen). However, looking at the fits given in Section 4, there is no significant change in the short range atomic structure as a function of annealing temperature.

The mechanical loss of tantala based coatings has been shown to change significantly as a function of annealing temperature [8]. We postulate that, given these significant changes in the mechanical loss with annealing temperature and the observation of only subtle changes in the short range order, it is more likely the medium range order (∼1-5 nm range) will show considerable changes as a function of annealing temperature. Initial investigations using fluctuation electron microscopy (FEM) have proven the existence of medium range order in tantala coatings [23], which could indicate the presence of a paracrystalline structure of tantala, and studies are ongoing to determine the nature and extent of medium range order change as a function of annealing temperature.

In NMR studies of IBS and sol-gel titania-tantala mixtures [13, 22, 24, 25], it is seen that the sol-gel and IBS films have similar co-ordination environments where the titanium atoms prefer to form complexes with 3-coordinated oxygen atoms. Combined with our data, it is possible that the second shell location where the titanium atoms prefer to sit within the Bassiri model represents the sites that are associated with these higher-coordinated oxygen atoms. The growth of the peak associated with the titanium atoms matches with the increase of oxygen coordination seen in the NMR studies. Although, as previously mentioned, there is some disagreement with the first shell oxygen co-ordination as titania concentration is increased: the first shell oxygen atom shows a statistically signifi-

cant decreasing co-ordination in the EXAFS data of IBS films, but in NMR investigations of sol-gel the oxygen coordination shows an increasing trend. This could be addressed in the future by experimentally studying identical thin film samples, and atomic modeling which takes into account both data sets.

The second nearest neighbor distributions (metal-metal distances) changes significantly as titania concentration increases, where the titanium atoms (Ti1 distance) gathers close to the Ta1 distances and becomes the predominant feature, see Fig. 3. It is therefore natural to assume that mixing with titania adds additional constraints on the structure compared to a pure tantala sample, and therefore increases the constraints in the two-level systems that are responsible for the mechanical loss. This would be evidenced by an increase in the average activation energy for the loss mechanisms and a reduced mechanical loss. Previous studies have found some evidence of both of these effects when comparing the temperature dependence of the mechanical loss of tantala mixed with 14.5 % Ti [9, 26].

In the future, the EXAFS data obtained within this study may be used to improve various atomic models used for predicting the mechanical properties of titania-tantala mixtures. Such models have already been developed using *ab initio* calculations [11, 12] and Transmission Electron Microscopy measurements [14, 15]. The addition of element-specific short-range structure provided by EXAFS will enhance the atomic models and lead to new insights into the mechanical loss mechanisms and other mechanical properties of these films.

6. Conclusion

We have measured the structure of mixtures of titania and tantala at various annealing temperatures using Ta L_{III} and Ti K edge EXAFS. From these data, we can conclude that post-deposition annealing produces only subtle changes in the short-range atomic structure, apart from the partial crystallization of the 68% Ti 600°C sample. The titania-tantala mixtures maintain a structure similar to that of pure tantala, with the Ti atoms being preferentially located at the second shell distance, which is similar to the Ta-Ta distance seen in the pure tantala structure.

Ultimately, this research indicates the following results:

1. Post deposition annealing does not greatly affect the titania-tantala structure. From the Ta L_{III} data, the changes with increasing annealing temperature are subtle in the $\chi(R)$ and $\chi(k)$ data, and are impossible to extract using the fit to the model discussed in this paper due to large uncertainty in the parameter values. There is some evidence for these subtle structural changes, such as the sharpening of some peaks with increased annealing temperatures (visible in Fig. 4).
2. Ti prefers the second-shell location. The only location where a Ti atom can fit when applying the pure tantala model to the Ti:Ta_2O_5 data is in the second shell, where the shortest Ta-Ta path lies. As expected, the NS_0^2 value for the Ta-Ti path (Ti1) in the Ta L_{III} data increases with increasing titania concentration.
3. Increased titania concentration mostly affects the second and third shells of the tantala structure. It is also noticed that there may be a small decrease in the number of oxygen atoms in the third shell (O3) with increased titania concentration. This might be expected due to the lower coordination number of Ti atoms.
4. The Ti and Ta atoms have similar locations and responses in the EXAFS spectra, making it difficult to differentiate between the two metal cations in the second shell.

The next step in this research is to study the medium-range order through TEM [23] and grazing incidence X-ray pair distribution function measurements. Also, these measurements can be used to refine atomic models used in predicting macroscopic behavior [11, 12].

Acknowledgments

This research was supported by the National Science Foundation, award number PHY-1404430. The LIGO Laboratory operates under co-operative agreement PHY-0107417. Use of the Stanford Synchrotron Radiation Lightsource, SLAC National Accelerator Laboratory, is supported by the U.S. Department of Energy, Office of Science, Office of Basic Energy Sciences under Contract No. DE-AC02-76SF00515. SR holds a Royal Society (RS) Wolfson Research Merit award. IWM is supported by a RS University Research Fellowship. This paper has been assigned LIGO Document Number LIGO-P1500183. The authors would like to thank colleagues in the LIGO Scientific Collaboration for many useful discussions and their support of this research.

[1] N. Kaiser, H. Pulker, Optical Interference Coatings, Springer Series in Optical Sciences, Springer Berlin Heidelberg, 2003.
[2] Y. Y. Jiang, A. D. Ludlow, N. D. Lemke, R. W. Fox, J. A. Sherman, L. S. Ma, C. W. Oates, Making optical atomic clocks more stable with 10^{16}-level laser stabilization, Nat. Photonics 5 (3) (2011) 158–161.
[3] D. Andrews, S. Roden, T. King, A model for lock-in growth in ring laser gyroscopes, IEEE J. Quantum Elect. 31 (9) (1995) 1709 –1715.
[4] K. Numata, A. Kemery, J. Camp, Thermal-noise limit in the frequency stabilization of lasers with rigid cavities, Phys. Rev. Lett. 93 (2004) 250602.
[5] T. Kessler, T. Legero, U. Sterr, Thermal noise in optical cavities revisited, J. Opt. Soc. Am. B 29 (1) (2012) 178–184.
[6] T. L. S. Collaboration, Advanced LIGO, Classical Quant. Grav. 32 (7) (2015) 074001.
[7] G. M. Harry, H. Armandula, E. Black, D. R. M. Crooks, G. Cagnoli, J. Hough, P. Murray, S. Reid, S. Rowan, P. Sneddon, M. M. Fejer, R. Route, S. D. Penn, Thermal noise from optical coatings in gravitational wave detectors, Appl. Opt. 45 (7) (2006) 1569–1574.

[8] I. W. Martin, R. Bassiri, R. Nawrodt, M. M. Fejer, A. Gretarsson, E. Gustafson, G. Harry, J. Hough, I. MacLaren, S. Penn, S. Reid, R. Route, S. Rowan, C. Schwarz, P. Seidel, J. Scott, A. L. Woodcraft, Effect of heat treatment on mechanical dissipation in Ta_2O_5 coatings, Classical Quant. Grav. 27 (22) (2010) 225020.

[9] I. W. Martin, E. Chalkley, R. Nawrodt, H. Armandula, R. Bassiri, C. Comtet, M. M. Fejer, A. Gretarsson, G. Harry, D. Heinert, J. Hough, I. MacLaren, C. Michel, J.-L. .Montorio, N. Morgado, S. Penn, S. Reid, R. Route, S. Rowan, C. Schwarz, P. Seidel, W. Vodel, A. L. Woodcraft, Comparison of the temperature dependence of the mechanical dissipation in thin films of Ta_2O_5 and Ta_2O_5 doped with TiO_2, Classical Quant. Grav. 26 (15) (2009) 155012.

[10] P. J. Martin, A. Bendavid, M. V. Swain, R. P. Netterfield, T. J. Kinder, W. G. Sainty, D. Drage, Mechanical and optical properties of thin films of tantalum oxide deposited by ion-assisted deposition, Mater. Res. Soc. Symp. P. 306 (1993) 583.

[11] J. P. Trinastic, R. Hamdan, Y. Wu, L. Zhang, H.-P. Cheng, Unified interatomic potential and energy barrier distributions for amorphous oxides, J. Chem. Phys. 139 (15) (2013) 154506.

[12] R. Hamdan, J. P. Trinastic, H. P. Cheng, Molecular dynamics study of the mechanical loss in amorphous pure and doped silica, J. Chem. Phys. 141 (5) (2014) 054501.

[13] N. Kim, J. F. Stebbins, Effects of annealing on the structure of ion beam sputtered amorphous tantalum oxide: Oxygen-17 NMR spectra and relaxation times, J. Non-Cryst. Solids 378 (2013) 158–162.

[14] R. Bassiri, K. B. Borisenko, D. J. H. Cockayne, J. Hough, I. MacLaren, S. Rowan, Probing the atomic structure of amorphous Ta_2O_5 coatings, Appl. Phys. Lett. 98 (3) (2011) 031904.

[15] R. Bassiri, K. Evans, K. Borisenko, M. Fejer, J. Hough, I. MacLaren, I. Martin, R. Route, S. Rowan, Correlations between the mechanical loss and atomic structure of amorphous TiO_2-doped Ta_2O_5 coatings, Acta Mater. 61 (4) (2013) 1070 – 1077.

[16] R. Bassiri, F. Liou, M. R. Abernathy, N. Kim, A. C. Lin, A. Mehta, B. Shyam, R. L. Byer, E. K. Gustafson, M. Hart, I. MacLaren, I. W. Martin, R. K. Route, S. Rowan, J. F. Stebbins, M. M. Fejer, Order within disorder: The atomic structure of ion-beam sputtered amorphous tantala (a-Ta_2O_5), APL Materials 3 (2015) 036103.

[17] B. Ravel, M. Newville, ATHENA, ARTEMIS, HEPHAESTUS: data analysis for X-ray absorption spectroscopy using IFEFFIT, J. Synchrotron Radiat. 12 (4) (2005) 537–541.

[18] M. Newville, IFEFFIT: interactive XAFS analysis and FEFF fitting, J. Synchrotron Radiat. 8 (2) (2001) 322–324.

[19] S. Calvin, E. Carpenter, B. Ravel, V. Harris, S. Morrison, Multiedge refinement of extended x-ray-absorption fine structure of manganese zinc ferrite nanoparticles, Phys. Rev. B 66 (22) (2002) 224405.

[20] B. Lengeler, P. Eisenberger, Extended x-ray absorption fine structure analysis of interatomic distances, coordination numbers, and mean relative displacements in disordered alloys, Phys. Rev. B 21 (1980) 4507–4520.

[21] S. Calvin, XAFS for Everyone, CRC Press, 2013.

[22] N. Kim, R. Bassiri, M. M. Fejer, J. F. Stebbins, The structure of ion beam sputtered amorphous alumina films and effects of Zn doping: High-resolution ^{27}Al NMR, J. Non-Cryst. Solids 405 (0) (2014) 1 – 6.

[23] R. Bassiri, M. Hart, R. L. Byer, K. B. Borisenko, K. Evans, M. M. Fejer, A. C. Lin, I. MacLaren, A. S. Markosyan, I. W. Martin, R. K. Route, S. Rowan, Investigating the medium range order in amorphous Ta_2O_5 coatings, J. Phys.: Conf. Ser. 522 (1) (2014) 012043.

[24] N. Kim, J. F. Stebbins, Structure of Amorphous Tantalum Oxide and Titania-Doped Tantala: ^{17}O NMR Results for Sol–Gel and Ion-Beam-Sputtered Materials, Chem. Mater. 23 (15) (2011) 3460–3465.

[25] N. Kim, J. F. Stebbins, LIGO Document G1300289 (unpublished).

[26] I. Martin, H. Armandula, C. Comtet, M. M. Fejer, A. Gretarsson, G. Harry, J. Hough, J.-M. M. Mackowski, I. MacLaren, C. Michel, J.-L. .Montorio, N. Morgado, R. Nawrodt, S. Penn, S. Reid, A. Remillieux, R. Route, S. Rowan, C. Schwarz, P. Seidel, W. Vodel, A. Zimmer, Measurements of a low-temperature mechanical dissipation peak in a single layer of Ta_2O_5 doped with TiO_2, Classical Quant. Grav. 25 (5) (2008) 055005.